CELLULAR NEUROSCIENCE

New neurons use Slit-Robo signaling to migrate through the glial meshwork and approach a lesion for functional regeneration

N. Kaneko[1], V. Herranz-Pérez[2,3]*, T. Otsuka[4,5]*, H. Sano[5,6]*, N. Ohno[7,8]*, T. Omata[1], H. B. Nguyen[8,9], T. Q. Thai[8], A. Nambu[5,6], Y. Kawaguchi[4,5], J. M. García-Verdugo[2], K. Sawamoto[1,10]†

After brain injury, neural stem cell–derived neuronal precursors (neuroblasts) in the ventricular-subventricular zone migrate toward the lesion. However, the ability of the mammalian brain to regenerate neuronal circuits for functional recovery is quite limited. Here, using a mouse model for ischemic stroke, we show that neuroblast migration is restricted by reactive astrocytes in and around the lesion. To migrate, the neuroblasts use Slit1-Robo2 signaling to disrupt the actin cytoskeleton in reactive astrocytes at the site of contact. Slit1-overexpressing neuroblasts transplanted into the poststroke brain migrated closer to the lesion than did control neuroblasts. These neuroblasts matured into striatal neurons and efficiently regenerated neuronal circuits, resulting in functional recovery in the poststroke mice. These results suggest that the positioning of new neurons will be critical for functional neuronal regeneration in stem/progenitor cell–based therapies for brain injury.

INTRODUCTION

The potential treatment of brain diseases by neuronal regeneration therapy using endogenous neural stem cells has gained attention in recent years. While most neurons are generated by neural stem cells during embryonic brain development, new neuron production continues in the postnatal ventricular-subventricular zone (V-SVZ) of various animals (*1*). In olfaction, the immature new neurons, called neuroblasts, form chain-like aggregates that migrate through a pathway called the rostral migratory stream (RMS) toward the olfactory bulb, the primary center of the olfactory system, where they differentiate into interneurons (*2*, *3*). Using a rodent ischemic stroke model induced by transient occlusion of the middle cerebral artery, we and others reported that some V-SVZ–derived neuroblasts migrate toward the lesion in the lateral striatum, where they mature and become integrated into the neuronal circuitry (*4*–*6*). However, these new neurons cannot restore sufficient neuronal function.

Within a few days after stroke, astrocytes, a major population of macroglia, in and around the area with neuronal loss, become "reactive astrocytes," with a larger soma, thicker processes, and proliferative behavior. The reactive astrocytes are a major component of glial scars, which have distinct roles in the pathogenesis, protection, and/or regeneration of injured brain tissues, depending on circumstances (*7*, *8*). Although reactive astrocytes are reported to promote neurogenesis in the poststroke striatum (*9*, *10*), their role in neuronal migration is unknown. Here, using a mouse model for ischemic stroke, we demonstrated that neuroblasts move toward the lesion using Slit1-Robo2 signaling to migrate through the meshwork of reactive astrocytes. Overexpressing (OE) *Slit1* in the neuroblasts increased their migration toward the lesion, which resulted in the positioning of mature new neurons closer to the injured area, and promoted functional recovery after stroke.

RESULTS

Reactive astrocytes restrict neuroblast migration toward the lesion in the poststroke brain

We first examined the detailed spatial relationship between the chain-forming neuroblasts and their surrounding astrocytes using the three-dimensional (3D) reconstruction of serial block-face scanning electron microscopy (SBF-SEM) images. The chain of neuroblasts made extensive contact with the astrocytic processes (Fig. 1A, fig. S1A, and movie S1), suggesting that reactive astrocytes are involved in neuronal migration through direct contact.

We next examined the distribution of migrating neuroblasts in the 12-, 18-, and 35-day poststroke striatum, which is enriched with reactive astrocytes, by immunohistochemistry (Fig. 1, B to D). Reactive astrocytes, identified by their strong expression of glial fibrillary acidic protein (GFAP), were broadly distributed in and around the injured lateral striatum, including the areas without neuronal loss. The neuroblasts were counted in the area lacking reactive astrocytes (reactive astrocyte free) and in the reactive astrocyte–rich area at four different distances (0 to 100 μm, 100 to 200 μm, 200 to 500 μm, and >500 μm) from the boundary between the areas with and without reactive astrocytes. The results showed that neuroblasts accumulated in the area <200 μm from the boundary at all time points (Fig. 1D),

[1]Department of Developmental and Regenerative Biology, Nagoya City University Graduate School of Medical Sciences, 1 Kawasumi, Mizuho-cho, Mizuho-ku, Nagoya, Aichi 467-8601, Japan. [2]Laboratory of Comparative Neurobiology, Instituto Cavanilles, Universidad de Valencia, CIBERNED, C/Catedrático José Beltrán, 2, Paterna, 46980 Valencia, Spain. [3]Predepartamental Unit of Medicine, Faculty of Health Sciences, Universitat Jaume I, Q-6250003-H Av. de Vicent Sos Baynat, s/n, 12071 Castelló de la Plana, Spain. [4]Division of Cerebral Circuitry, National Institute for Physiological Sciences, 5-1 Higashiyama, Myodaiji, Okazaki, Aichi 444-8787, Japan. [5]Department of Physiological Sciences, SOKENDAI (The Graduate University for Advanced Studies), Okazaki, Aichi 444-8585, Japan. [6]Division of System Neurophysiology, National Institute for Physiological Sciences, 38 Nishigonaka, Myodaiji, Okazaki, Aichi 444-8585, Japan. [7]Department of Anatomy, Division of Histology and Cell Biology, Jichi Medical University, School of Medicine, 3311-1 Yakushiji, Shimotsuke, Tochigi 329-0498, Japan. [8]Division of Neurobiology and Bioinformatics, National Institute for Physiological Sciences, 5-1 Higashiyama, Myodaiji, Okazaki, Aichi 444-8787, Japan. [9]Department of Anatomy, Faculty of Medicine, University of Medicine and Pharmacy (UMP), Ho Chi Minh City 700000, Vietnam. [10]Division of Neural Development and Regeneration, National Institute for Physiological Sciences, 5-1 Higashiyama, Myodaiji, Okazaki, Aichi 444-8787, Japan.
*These authors contributed equally to this work.
†Corresponding author. Email: sawamoto@med.nagoya-cu.ac.jp

suggesting that the neuroblast migration was perturbed after entering the reactive astrocyte–rich area.

To examine the response of migrating neuroblasts making contact with reactive astrocytes, we performed time-lapse imaging of poststroke *Gfap-EGFP;Dcx-DsRed* mouse brain slices in which astrocytes and neuroblasts were labeled with enhanced green fluorescent protein (EGFP; green) and discosoma red fluorescent protein (DsRed, red), respectively (movie S2). When the neuroblasts reached

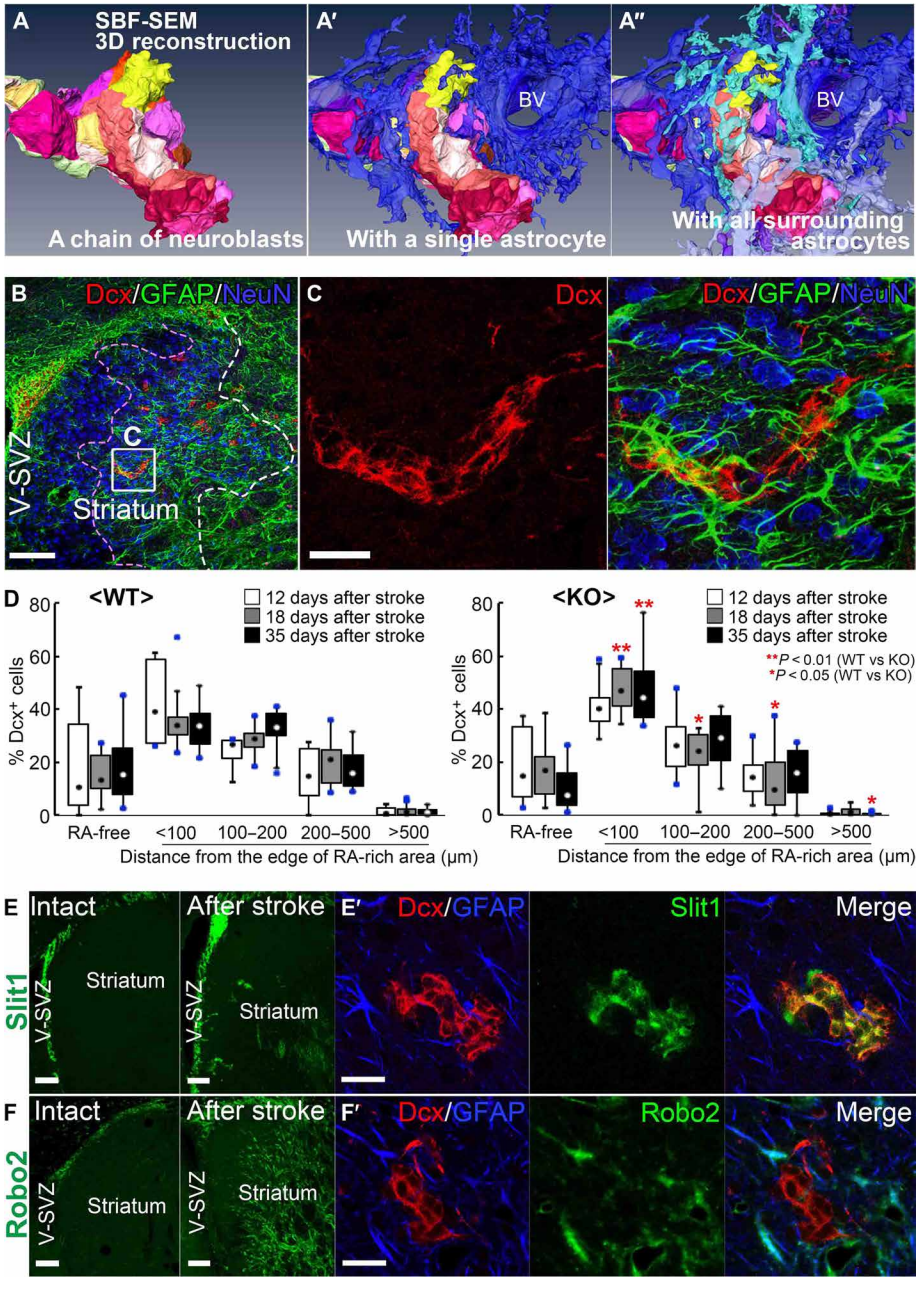

Fig. 1. Reactive astrocytes inhibit the ability of neuroblasts to approach the lesion in the poststroke brain. 3D reconstruction of SBF-SEM images of a chain of neuroblasts (**A**) in the poststroke striatum and the same chain with a single (**A′**) or all (**A″**) of the surrounding astrocytes tightly enwrapping an adjacent blood vessel (BV). (**B** and **C**) *Z*-stacked confocal images of neuroblasts (Dcx, red), astrocytes (GFAP, green), and mature neurons (NeuN, blue) in an 18-day poststroke brain section. Panels in (C) are higher-magnification images of the neuroblast chain boxed in (B). The white broken line in (B) indicates the boundary of the infarct area. The pink broken line in (B) indicates the boundary of the reactive astrocyte–rich and –free areas. (**D**) Distribution of Dcx^+ neuroblasts in the reactive astrocyte (RA)–free area and the reactive astrocyte–rich area at different distances from the reactive astrocyte–free and reactive astrocyte–rich border (<100, 100 to 200, 200 to 500, and >500 μm lateral to the boundary) in 12-day [wild-type (WT), $n = 6$ mice; knockout (KO), 11 mice], 18-day (WT, $n = 14$ mice; KO, $n = 12$ mice), and 35-day poststroke mice (WT, $n = 17$ mice; KO, $n = 10$ mice). Comparison among the time points (12, 18, and 35 days): one-way analysis of variance (ANOVA); comparison between WT and KO: two-tailed unpaired *t* test. (**E** and **F**) Localization of Slit1 and Robo2 in intact and 18-day poststroke striatum. Higher-magnification images (**E′** and **F′**) show Dcx^+ neuroblasts (red) and $GFAP^+$ reactive astrocytes (blue), which expressed Slit1 and Robo2 (green), respectively. Box plots show the median (dot), upper and lower quartiles (box), maximal and minimal values excluding outliers (whiskers), and outliers (blue squares). $^*P < 0.05$, $^{**}P < 0.01$. Scale bars, 100 μm (B, E, and F) and 20 μm (C, E′, and F′).

the areas enriched with reactive astrocytes, they slowed down, frequently changed direction, and increased their resting period without changing the cycle length of their saltatory migration, compared with neuroblasts in the area lacking reactive astrocytes or in the RMS (fig. S1, B to E). These observations collectively suggested that the reactive astrocytes inhibit the neuroblasts' ability to approach the lesion.

Neuroblasts use Slit-Robo signaling to migrate through the meshwork of reactive astrocytes

We previously reported that neuroblasts in the postnatal RMS use a diffusive protein, Slit1, to control the morphology of surrounding astrocytes through Slit1's receptor, Robo2, enabling their rapid migration toward the olfactory bulb (*11*). Under physiological conditions, migrating neuroblasts in the V-SVZ and RMS express Slit1, and the surrounding astrocytes, but not those in other brain regions including the striatum, express Robo2 (Fig. 1, E and F, intact). In the 18-day poststroke brain, neuroblasts migrating toward the lesion also expressed Slit1 (Fig. 1, E and E′), although the expression level was significantly lower than that in neuroblasts of the V-SVZ and progressively decreased as the neuroblasts got further away from the V-SVZ (fig. S1, F and G). We observed a similar rapid down-regulation in the expression of doublecortin (Dcx) in the neuroblasts migrating toward the lesion (fig. S1H) and of Slit1 and Dcx in neuroblasts leaving the RMS in the olfactory bulb (fig. S1, I and J). Notably, after stroke, strong Robo2 expression was induced in the reactive astrocytes, but not in neuroblasts in the striatum (Fig. 1, F and F′). The *Robo2* mRNA level, along with the *GFAP* mRNA level, was significantly higher in astrocytes isolated from the ipsilateral striatum of the *Gfap-EGFP* mouse by laser microdissection, compared with those from the contralateral striatum (fig. S1, K and L). These expression patterns suggested that the neuroblast-derived Slit1 could regulate Robo2-expressing astrocytes in the poststroke striatum.

To investigate Slit1's role in neuronal migration toward the lesion, we compared the neuroblast migration in *Slit1*-intact [control (Cnt)] and *Slit1*-KO mice by Dcx immunohistochemistry (Fig. 2, A and B) and time-lapse imaging (Fig. 2, C to E, and movie S3) of the poststroke striatum, which was enriched with reactive astrocytes. In the 18-day poststroke mouse brain, most of the neuroblasts were distributed in the area <500 μm from the V-SVZ, even in the Cnt mice. The proportion of neuroblasts accumulated in the striatum <100 μm from the V-SVZ was significantly higher in the KO than in the Cnt mice (Fig. 2, A and B), while the total number of neuroblasts migrating into the striatum (WT, 5210 ± 1590 cells, $n = 12$ mice; KO, 2370 ± 630 cells, $n = 15$ mice; $P > 0.05$) and the stroke-induced increase in V-SVZ cell proliferation were not significantly different between the Cnt and *Slit1*-KO groups (fig. S2, A to C). We then examined the spatial relationship between reactive astrocytes and the neuroblast accumulation in KO mice fixed at different poststroke time points (12, 18, and 35 days). More than 40% of the KO neuroblasts were accumulated in the area <100 μm inside the reactive astrocyte–rich area at all time points (Fig. 1D). Time-lapse imaging revealed that the migration speed of neuroblasts in the reactive astrocyte–rich areas of the striatum was significantly lower than that in the reactive astrocyte–absent area in both the Cnt and KO brains (Fig. 2C). The mean migration speed and mean dynamics and length of the leading process in *Slit1*-KO neuroblasts were significantly decreased compared with those of the Cnt group in the reactive astrocyte–rich area, but not in the reactive astrocyte–absent area (Fig. 2, C to E), suggesting that astrocytes can inhibit neuroblast migration regardless of the presence of Slit1 expression in neuroblasts and that Slit1 helps neuroblasts migrate through these astrocytes. Electron microscopy revealed that in the WT poststroke striatum, astrocytic processes surrounded and made direct contact with the chains of migrating neuroblasts but did not project into the chains, similar to those observed in the normal RMS (*11*, *12*). However, in the *Slit1*-KO mice, astrocytic processes were irregularly inserted into the chains and made excessive contact with the neuroblasts (Fig. 2, F and G). Similar impaired migration was observed in *Slit1*-KO neuroblasts transplanted into poststroke WT (Fig. 2, H to K) or *Slit1*-KO (fig. S2, D and E) medial striatum. Next, to test the effect of knocking down *Robo2* in striatal cells on neuroblast migration, we injected a lentivirus encoding *Robo2*–short hairpin RNA (shRNA) or nonsilencing Cnt shRNA along with turbo-GFP into WT mouse striatum 2 days before stroke induction. At 18 days after stroke, the turbo-GFP expression in the reactive astrocyte–rich area was observed mainly in $GFAP^+$ astrocytes (about 70%) and sparsely in other cell types (less than 10% each), which were positive for Iba1 (microglial marker), NeuN (mature neuronal marker), CD31 (endothelial cell marker), Olig2 (oligodendrocyte-lineage marker), or Dcx (fig. S2, F and G). The neuroblast migration was significantly impaired in the striatum treated with Robo2-knockdown lentivirus compared with that with Cnt shRNA lentivirus (Fig. 2, L to O). These observations indicated that the neuroblasts use Slit1 to migrate through the meshwork of Robo2-expressing reactive astrocytes, although the Slit1 expression level gradually decreases during their migration toward the lesion (fig. S1, F and G).

To directly demonstrate the inhibitory role of astrocytes in neuroblast migration, we performed an in vitro experiment. Slit1-expressing (Cnt) and *Slit1*-KO V-SVZ neuroblasts were embedded in collagen gel with or without striatal astrocytes that had been exposed to transient hypoxia, which significantly increases the expression levels of *GFAP* and *Robo2* within 4 days (fig. S2, H and I), similar to reactive astrocytes in vivo (Fig. 1, B and F, and fig. S1, K and L). We then measured the neuroblasts' migration distance 2 days later. Both Cnt and KO neuroblasts showed a significantly shorter migration distance in the astrocyte-containing gel than in the astrocyte-free gel, indicating that astrocytes can inhibit neuroblast migration regardless of the presence of Slit1 expression in the neuroblasts (fig. S2, J and K). The migration distance of the KO neuroblasts was significantly shorter than that of the Cnts only in the astrocyte-containing gels, suggesting that Slit1 helps neuroblasts migrate through the astrocytes.

Neuroblasts frequently migrate along blood vessels in the poststroke striatum (*6*, *13*–*15*). As blood vessels are tightly enwrapped by surrounding astrocytes, neuroblasts directly interact with astrocytes when they migrate along the vascular scaffolds (Fig. 1, A and A″, and movie S1) (*6*, *13*, *16*). Therefore, we observed 18-day poststroke brain sections stained for the vascular endothelial cell marker, CD31, and Dcx. There was no significant difference in the density of blood vessels in the striatum between the WT and *Slit1*-KO groups in the pre- or poststroke brain (fig. S2, L and M). However, in contrast to the WT neuroblasts, which formed chain-like elongated clusters along the vessels, *Slit1*-deficient neuroblasts frequently formed globular aggregates with an irregular morphology when in contact with blood vessels (fig. S2N), suggesting that the Slit1-mediated mechanism to move in contact with reactive astrocytes is also necessary for the blood vessel–guided migration of neuroblasts in the poststroke brain.

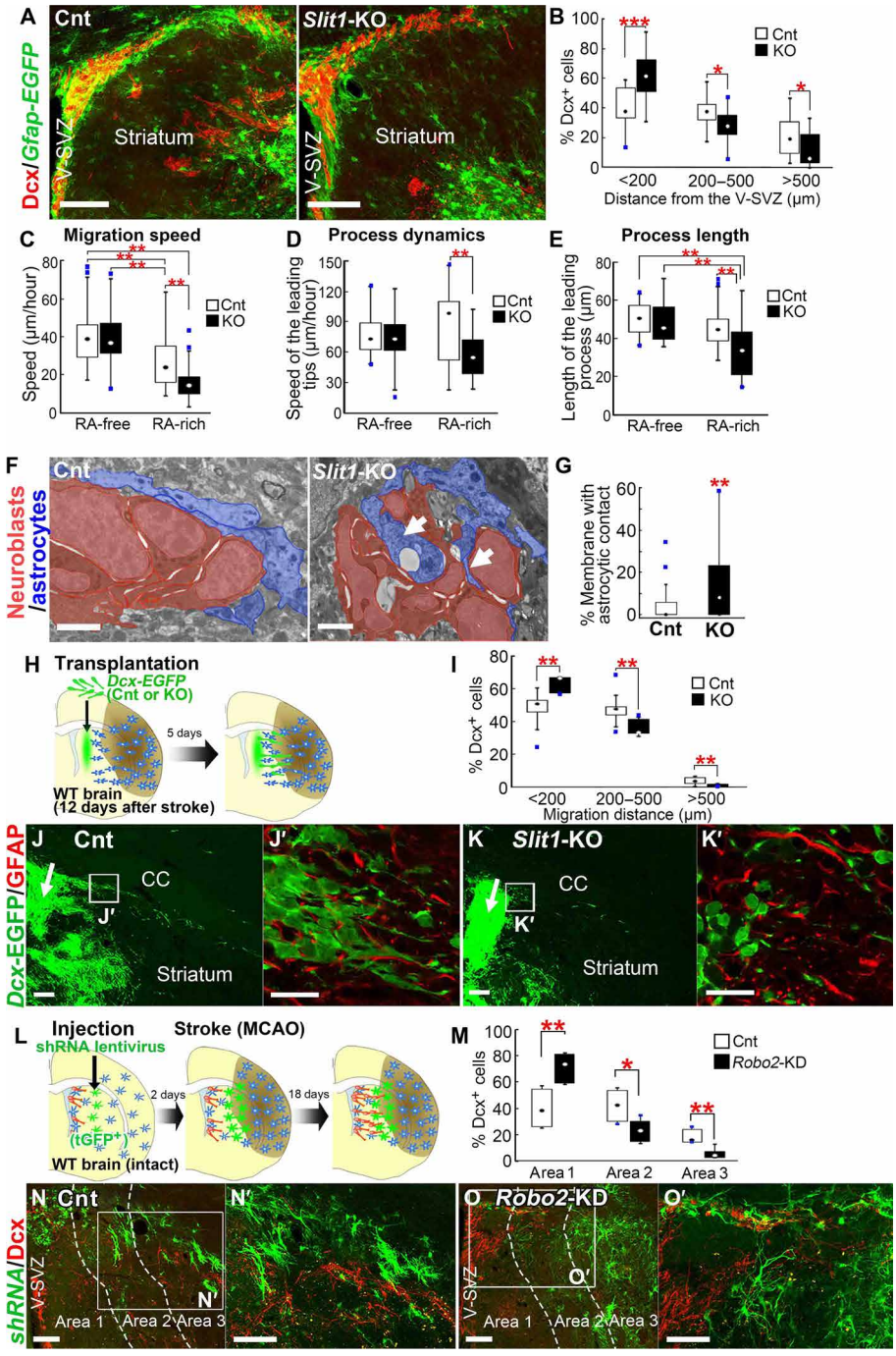

Fig. 2. Slit-Robo signaling controls neuronal migration through stroke-activated astrocytes. (**A** and **B**) Distribution of Dcx$^+$ neuroblasts in 18-day poststroke controls (Cnt) and *Slit1*-KO *Gfap-EGFP* mouse striatum. (B) shows the percentage of Dcx$^+$ neuroblasts in areas at different distances from the V-SVZ (two-tailed Mann-Whitney *U* test; Cnt, $n = 12$ mice; KO, $n = 15$ mice). (**C** to **E**) Quantitative analyses of the time-lapse imaging (movie S3) of migrating neuroblasts in the Cnt and *Slit1*-KO poststroke striatum, which was enriched with reactive astrocytes. Graphs show the migration speed [C, Steel-Dwass test; reactive astrocyte (RA)–free area: Cnt, $n = 77$ cells; KO, $n = 56$ cells; reactive astrocyte–rich area: Cnt, $n = 99$ cells; KO, $n = 97$ cells] and the moving speed (D) and length (E) of the leading process (two-tailed one-way ANOVA and Bonferroni test; reactive astrocyte–free: Cnt, $n = 14$ cells; KO, $n = 19$ cells; reactive astrocyte–rich: Cnt, $n = 24$ cells; KO, $n = 23$ cells). (**F** and **G**) Electron microscopy of neuroblast chains (red) and their surrounding astrocytic processes (blue) in 14-day poststroke striatum (arrows indicate astrocytic processes inserted into the chain). (G) shows the percentage of the chain-forming neuronal membrane in contact with astrocytes (two-tailed Mann-Whitney *U* test; Cnt, $n = 36$ cells; KO, $n = 73$ cells). (**H** to **K′**) Distribution of *Slit1*-KO *Dcx-EGFP* neuroblasts (green) 5 days after transplantation into WT poststroke brain and their association with surrounding reactive astrocytes (red; two-tailed unpaired *t* test; Cnt, $n = 8$ mice; KO, $n = 7$ mice). (**L** to **O′**) Distribution of neuroblasts in the striatum with *Robo2*-knockdown astrocytes [area containing noninfected astrocytes (area 1) and areas enriched with shRNA-expressing astrocytes (area 2: <200 μm from area 1; area 3: ≥200 μm from area 1); two-tailed unpaired *t* test; Cnt, $n = 7$ mice; *Robo2*-knockdown (KD), $n = 6$ mice]. tGFP$^+$, turbo-GFP–positive. Box plots show the median (dot), upper and lower quartiles (box), maximal and minimal values excluding outliers (whiskers), and outliers (blue squares). *$P < 0.05$, **$P < 0.01$, ***$P < 0.001$. Scale bars, 100 μm (A, J, K, L, N, N′, O, and O′), 20 μm (J′ and K′), and 2 μm (F). MCAO, middle cerebral artery occlusion.

Neuroblasts maintain their migration route by controlling the astrocytes' actin cytoskeleton through Slit1-induced Cdc42 inactivation

In the 3D-reconstructed images of SBF-SEM data, we found that while many small protrusions were observed on the surface of reactive astrocytes without neuroblasts, those in contact with neuroblasts were smooth and free from protrusions (Fig. 3, A and A′), suggesting that neuroblasts control the protrusion formation on reactive astrocytes at their contact sites. To examine the effects of neuronal contact on the actin dynamics in astrocytes in detail (Fig. 3, B to J), we transfected hypoxia-activated striatal astrocytes with fluorescently labeled Lifeact, a filamentous (F)–actin–binding peptide (*17*), and cultured on a dish with Cnt or *Slit1*-KO neuroblasts. The astrocytes showed process retraction and a transient and local decrease in polymerized actin at the sites of contact with WT neuroblasts, but not with Slit1-deficient neuroblasts (Fig. 3, H and I; fig. S3A; and movie S4). Embedded in collagen gel, these astrocytes frequently formed small, thin F-actin–rich protrusions on the cell surface (Fig. 3, B and C), consistent with the morphology observed with SBF-SEM in vivo (Fig. 3A). In addition to the process retraction (Fig. 3D), the formation of these thin protrusions was also suppressed by contact with Slit1-expressing migrating neuroblasts (Fig. 3E). These results indicate that neuroblasts control the actin cytoskeleton of astrocytes at their sites of contact using Slit1.

As Slit-Robo signaling modifies the activity of Rho-family GTPases (guanosine triphosphatases), RhoA, Rac1, and Cdc42, to regulate actin polymerization in various cell types (*18*), we examined the dynamics of these activities in astrocytes at the contact site with migrating neuroblasts using fluorescence resonance energy transfer (FRET)–based biosensors (*19*). An increased activity of Cdc42, which is involved in astrocytic polarization in injured brain tissues (*20*), was observed at the tip of moving astrocyte processes on a dish (Fig. 3K, rectangles, and movie S5), and fine protrusions formed at the surface of astrocytes embedded in a collagen gel (movie S6). In addition, the Cdc42 activity was transiently suppressed by contact with WT, but not *Slit1*-KO neuroblasts (Fig. 3, K and L, and movie S7). Similar neuronal contact–induced GTPase activity changes in RhoA or Rac1 were not observed (fig. S3, B and C).

Furthermore, the *Slit1*-KO neuroblasts migrated significantly more slowly than Cnt neuroblasts in contact with astrocytes cultured on a dish (Fig. 3G). Cnt neuroblasts could not suppress the actin polymerization in astrocytes expressing a constitutively active Cdc42 mutant (CA-*Cdc42*; Fig. 3J and fig. S3, D to G), leading to a slower migration speed compared with those in contact with astrocytes expressing WT Cdc42 (Fig. 3G). These observations suggest that a transient decrease in Cdc42 activity, triggered by neuronal contact through Slit-Robo signaling, mediates rapid and dynamic changes in the actin cytoskeleton of reactive astrocytes to maintain the route for neuronal migration toward the lesion.

New neurons positioned close to the lesion by forced Slit1 expression promote functional recovery after stroke

Because most of the V-SVZ–derived neuroblasts stopped migrating at the area enriched with reactive astrocytes before reaching the area with stroke-induced neuronal loss (Fig. 1, B to D) and because they down-regulated Slit1 expression during their migration (fig. S1, F and G), we examined whether enhanced Slit1 expression in neuroblasts could promote their migration toward the lesion. We observed that V-SVZ–derived neuroblasts infected with lentivirus encoding Slit1 and the fluorescent protein Venus migrated faster in the poststroke striatum toward the injured area compared with those infected with Cnt lentivirus encoding Venus alone (fig. S4, A and B). To improve the infection efficiency, we treated dissociated V-SVZ cells with Slit1-OE or Cnt lentivirus and then transplanted them into the medial striatum of poststroke brains. The migration speed of the lentivirus-labeled cells with a monopolar/bipolar shape examined by time-lapse imaging (fig. S4, C to E, and movie S7) and the percentage of Dcx^+ neuroblasts that had migrated more than 200 μm toward the lesion in the brain sections fixed 8 days after transplantation (fig. S4, F and G) were significantly greater in the *Slit1*-overexpression group than in the Cnt group. *Slit1* overexpression did not alter the migration capacity of surrounding non–virus-treated cells dissociated from the Dcx-DsRed mouse V-SVZ, which had been mixed and cotransplanted with the virus-treated cells into the poststroke striatum, suggesting that *Slit1* overexpression promoted neuroblast migration in a cell-autonomous manner (fig. S4J). *Slit1* overexpression did not affect the proliferation of neuronal progenitors or the apoptosis of neuroblasts (fig. S4, H and I). These findings collectively indicated that the forced *Slit1* expression in neuroblasts increased their migration capacity toward the lesion.

We then investigated the final destination of the transplanted cells (Fig. 4) and their contribution to functional recovery (Fig. 5). We transplanted the lentivirus-labeled V-SVZ cells into the medial striatum at 8 days and then examined their differentiation into mature neurons at 35 days after stroke (Fig. 4A). While the transplanted cells that migrated into the olfactory bulb differentiated into $NeuN^+$ putative interneurons based on their morphology (fig. S4K), some of the cells distributed in the host striatum expressed the striatal projection neuron marker DARPP32 (Fig. 4B). The proportion of lentivirus-labeled cells that expressed DARPP32 was not significantly affected by Slit1 overexpression (Fig. 4B and fig. S4L). We also found small populations of lentivirus-labeled cells that expressed the striatal gamma-aminobutyric acid (GABA)ergic interneuron markers parvalbumin or calretinin, or the cholinergic interneuron marker choline acetyltransferase (Fig. 4, C and D, and fig. S4L); the proportions of these populations were comparable between the Cnt and Slit1-overexpression groups. In whole-cell patch-clamp recording of the lentivirus-labeled graft-derived cells with a neuronal morphology (smooth and oval cell bodies with neurites) in the poststroke striatum (Fig. 4, E to H), five of eight cells showed slowly developing depolarization and a long latency of spike generations in response to current pulse injections (Fig. 4, E and F), typical of the striatal projection neurons (medium-sized spiny neurons) (*21*, *22*). We observed spontaneous excitatory postsynaptic currents (sEPSCs) in these cells, suggesting that transplant-derived cells receive synaptic inputs from the cortex or thalamus (Fig. 4G). Electrophysiological properties of the transplant-derived cells were almost comparable to those of the host medium-sized spiny neurons, except for the input resistance, which was slightly but significantly higher in the transplant-derived cells (Fig. 4H). The intracellular labeling with biocytin revealed morphologies of recorded cells that have medium-sized soma and branched dendrites with many spines (Fig. 4, I to K), consistent with the previously reported morphology of striatal projection neurons (*21*, *23*). In addition, some of the transplant-derived new neurons were labeled with cholera toxin B (a retrograde axonal tracer) that had been injected into the globus pallidus, a major target area of the striatal projection neurons, suggesting that they projected their axons into that area (Fig. 4, L and M). Moreover, GFP immunogold electron microscopy

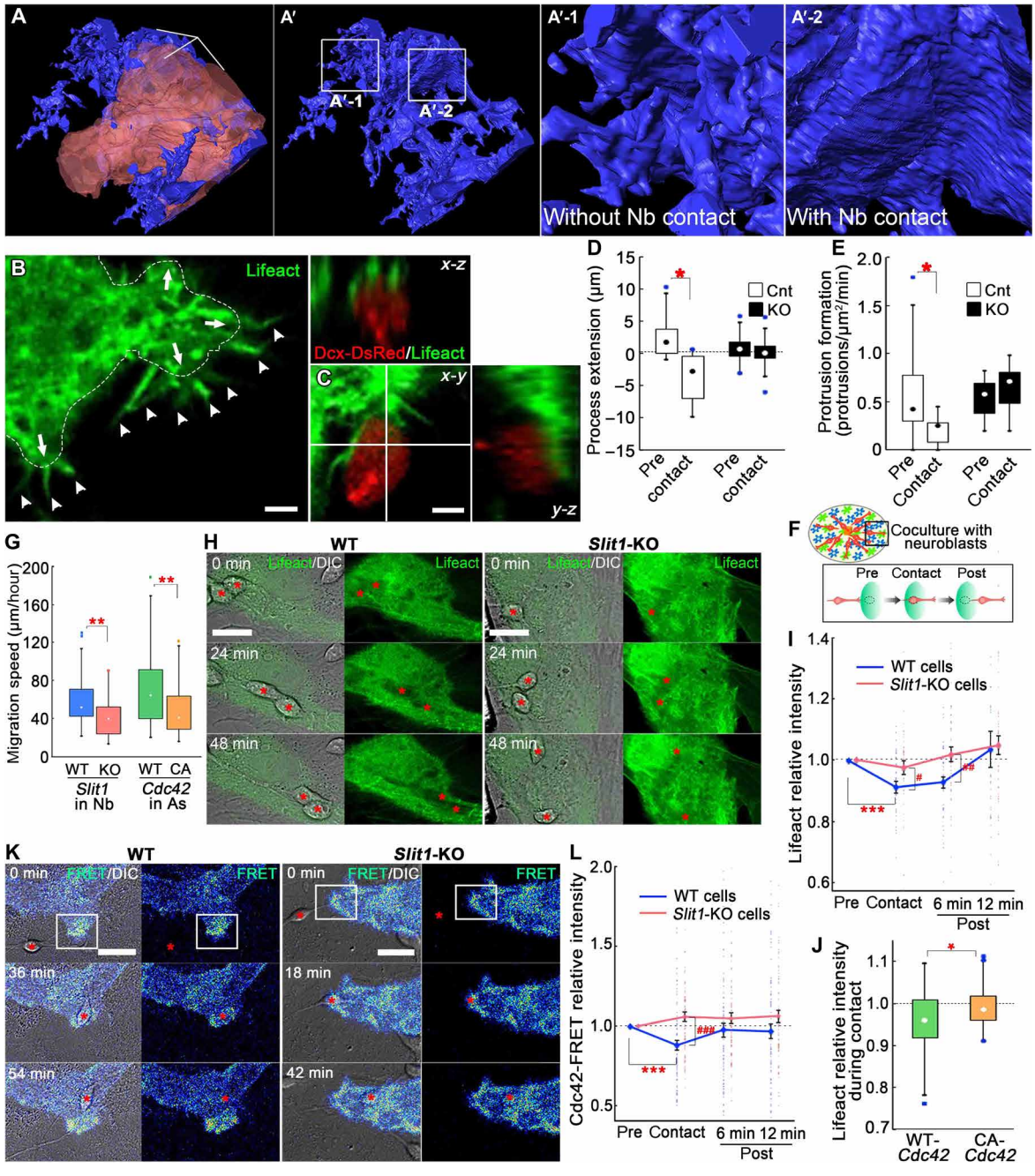

Fig. 3. Neuroblast-induced morphological dynamics of reactive astrocytes involve the inhibition of Cdc42-regulated actin polymerization. (**A**) 3D reconstruction of SBF-SEM images of the surface of reactive astrocytes (blue) surrounding a chain of neuroblasts (transparent pink). (**A′-1**) and (**A′-2**) show higher-magnification images of the boxed area. (**B** to **E**) Time-lapse imaging of F-actin visualized with Lifeact (green) in hypoxia-treated striatal astrocytes embedded in collagen gel with Dcx-DsRed neuroblasts (red) (C). (D) shows the extension of processes [arrowheads in (B)] for 18 min before (pre) and during/after neuroblast contact (two-tailed paired *t* test; Cnt, $n = 9$ areas; KO, $n = 10$ areas). (E) shows the frequency of F-actin–rich protrusion [arrowheads in (B)] formation at the surface of astrocytes before and during neuroblast contact (two-tailed paired *t* test; Cnt, $n = 9$ areas; KO, $n = 10$ areas). (**F**) Quantification procedure in (H) to (L). (**G**) Migration speed of neuroblasts in contact with hypoxia-treated astrocytes (two-tailed Mann-Whitney *U* test; WT neuroblasts, $n = 35$ cells; KO neuroblasts, $n = 32$ cells; WT-*Cdc42*, $n = 50$ cells; CA-*Cdc42*, $n = 51$ cells). (**H** and **I**) Time-lapse imaging of F-actin (Lifeact) in striatal astrocytes with migrating neuroblasts (asterisks) on a culture dish (H) and relative F-actin level in the astrocytes before, during, and after neuroblast contact (I) (WT, $n = 42$ areas; KO, $n = 45$ areas; within groups, Friedman test followed by pairwise comparison of Scheffé; WT versus KO, Mann-Whitney *U* test). (**J**) Relative F-actin level in astrocytes transfected with WT-*Cdc42* or CA-*Cdc42* during neuroblast contact (two-tailed unpaired *t* test; WT-Cdc42, $n = 37$ areas; CA-Cdc42, $n = 39$ areas). (**K** and **L**) Time-lapse imaging of Cdc42 biosensor-transfected astrocytes (rectangles, moving processes) with neuroblasts (asterisks) (K) and the relative Cdc42 activity in these astrocytes before, during, and after neuroblast contact (L) (WT, $n = 74$ areas; KO, $n = 73$ areas; within groups, Friedman test followed by pairwise comparison of Scheffé; WT versus KO, Mann-Whitney *U* test). Box plots show the median (dot), upper and lower quartiles (box), maximal and minimal values excluding outliers (whiskers), and outliers (blue squares). Dot plots show each value (small dots), and line graph values represent the mean ± standard error of the mean. $^{*}P < 0.05$, $^{**}P < 0.01$, $^{***}P < 0.001$, $^{\#}P < 0.05$, $^{\#\#}P < 0.01$, $^{\#\#\#}P < 0.001$. Scale bars, 20 μm (H and K) and 5 μm (A to C). Asterisk indicates a significant difference between Pre and each of the other time points in the same cell group; number sign indicates a significant difference between groups at one time point.

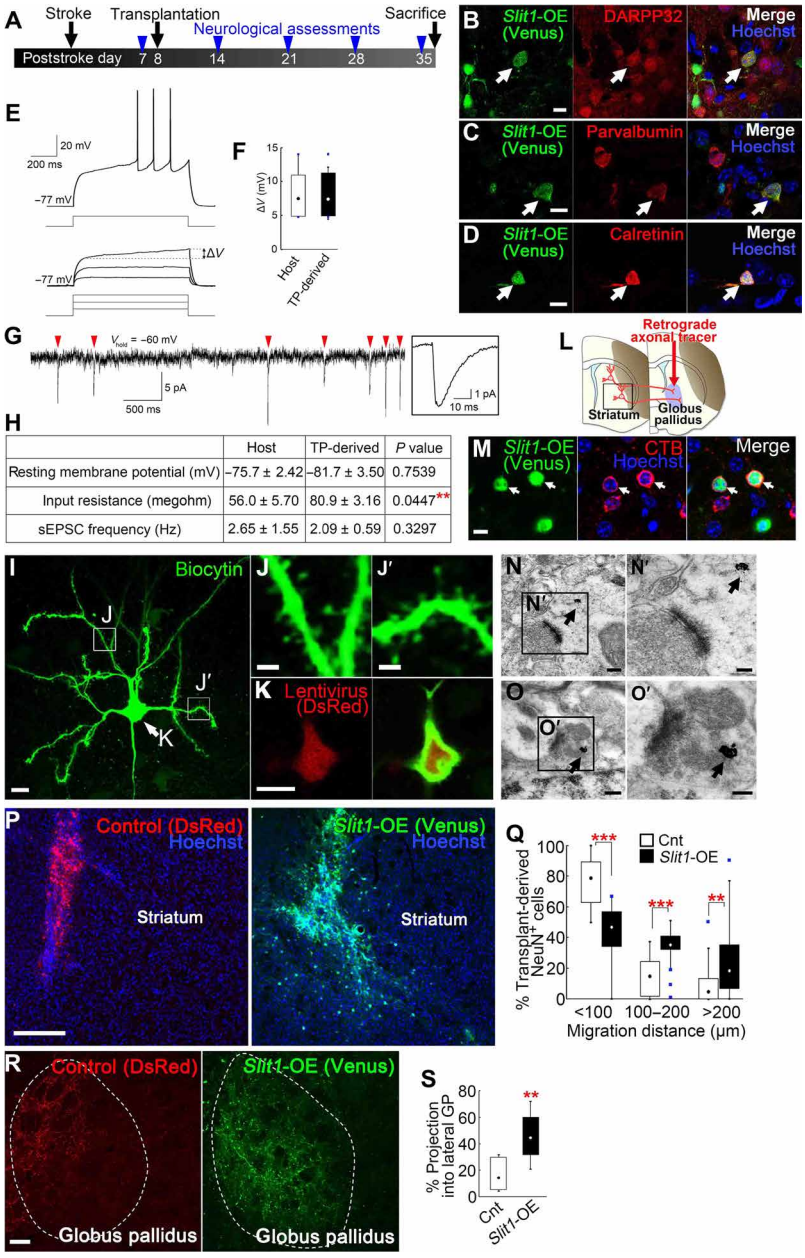

Fig. 4. Enhanced migration promotes neuronal regeneration around the lesion. (**A**) Experimental procedure. (**B** to **D**) Transplant-derived Slit1-OE cells expressing DARPP32, parvalbumin, and calretinin [arrows in (B) to (D)]. (**E** to **H**) Electrophysiological properties of transplant-derived neurons. In response to depolarizing current injection, transplant-derived cells showed early outward rectification and slowly developing ramp depolarization (E, bottom) (pulse amplitudes, 100, 200, and 300 pA) and a long latency to spike discharge (E, top) (pulse amplitude, 350 pA). (F) shows the change in voltage from the beginning (measured at 80 ms from the onset) to the end of a current injection just below spike threshold [ΔV in (E)] in transplant (TP)–derived and host neurons (two-tailed unpaired *t* test; transplanted, $n = 4$ cells; host, $n = 5$ cells). sEPSCs were observed in the transplant-derived cells (G) (the averaged sEPSC is presented in the box). (H) shows the comparison of the quantitative data between the transplant-derived and host striatal projection neurons (mean ± standard error of the mean, two-tailed unpaired *t* test). (**I** to **K**) Morphology of a transplant-derived striatal projection neuron intracellularly labeled with biocytin. Higher-magnification images of spiny dendrites (rectangles) and the lentivirus-labeled soma (arrow) are shown in (J), (J′), and (K), respectively. (**L** and **M**) Cholera toxin subunit B (CTB)–mediated labeling of Slit1-OE transplant-derived neurons projecting into the globus pallidus [arrows in (M)]. (**N** and **O**) Immunoelectron microscopy of synaptic structures formed by the transplant-derived cells. A postsynaptic area in the striatum (N) and a presynaptic area in the globus pallidus (O) labeled with gold particles (arrows) are shown. (**N′**) and (**O′**) are higher-magnification images of the boxed areas in (N) and (O), respectively. (**P** and **Q**) Percentage of NeuN colabeled transplanted cells distributed at various distances from the transplant site in the host striatum (Q) [Cnt (DsRed$^+$), $n = 20$ mice; *Slit1*-OE (Venus$^+$), $n = 21$ mice]. (**R** and **S**) Axonal projection of Cnt and *Slit1*-OE striatal new neurons into the globus pallidus, a major target area of the striatal projection neurons. *Slit1*-OE axons were more widely distributed throughout the globus pallidus compared with the Cnt axons (R). The percentage of projections into the lateral part of the globus pallidus was significantly higher in the *Slit1*-OE group (S) (two-tailed unpaired *t* test; Cnt, $n = 6$ mice; *Slit1*-OE, $n = 6$ mice). Box plots show the median (dot), upper and lower quartiles (box), maximal and minimal values excluding outliers (whiskers), and outliers (blue squares). $^{**}P < 0.01$, $^{***}P < 0.001$. Scale bars, 100 μm (P and R), 10 μm (B to D, I, K, and M), 2 μm (J), 0.2 μm (N and O), and 0.1 μm (N′ and O′).

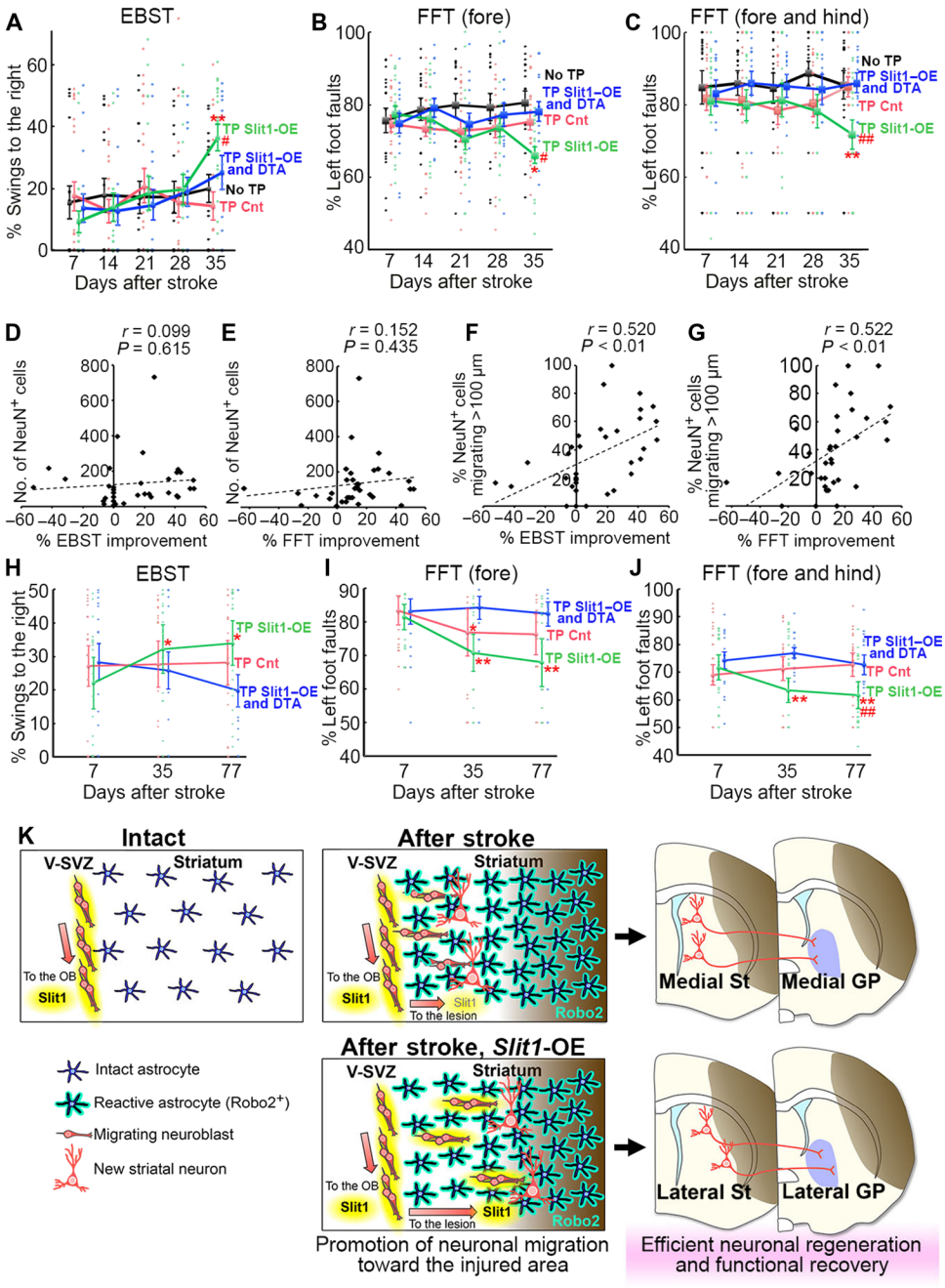

Fig. 5. Enhanced neuroblast migration promotes functional recovery. (**A** to **C**) Neurological assessments performed before (7 days after stroke) and 1 to 4 weeks after V-SVZ cell transplantation. The percentage of right swings in the elevated body swing test (EBST) (A) (Friedman test followed by pairwise comparison of Scheffé; transplant (TP) Cnt, $n = 20$ mice; TP *Slit1*-OE, $n = 19$ mice; no TP, $n = 16$ mice; TP Slit1–OE and DTA, $n = 15$ mice), the percentage of all forepaw slips that were left forepaw slips (B), and the percentage of all paw slips that were left forepaw and hindpaw slips (C) in the foot-fault test (FFT) (TP Cnt, $n = 20$ mice; TP *Slit1*-OE, $n = 19$ mice; no TP, $n = 16$ mice; TP Slit1–OE and DTA, $n = 15$ mice) are presented. Comparison between 7 and 35 days in each group: two-tailed Wilcoxon's signed-rank test, $^{*}P < 0.05$, $^{**}P < 0.01$; comparison between the no-TP group and every other group at 35 days: Steel test, $^{\#}P < 0.05$, $^{\#\#}P < 0.01$. (**D** to **G**) Scatterplots and regression lines showing the correlation of behavioral improvement in the elevated body swing test and foot-fault test with the total number of transplant-derived NeuN^{+} neurons (D and E) or the percentage of transplant-derived NeuN^{+} cells that moved more than 100 µm toward the injured area from the transplanted site (F and G) in each mouse ($n = 34$). (**H** to **J**) Neurological assessments performed before and 4 and 10 weeks after V-SVZ cell transplantation (7, 35, and 77 days after stroke, respectively). The percentage of right swings in the elevated body swing test (H) (Friedman test followed by pairwise comparison of Scheffé), the percentage of all forepaw slips that were left forepaw slips (I), and the percentage of all paw slips that were left forepaw and hindpaw slips (J) in the foot-fault test are presented (TP Cnt, $n = 19$ mice; TP *Slit1*-OE, $n = 20$ mice; TP Slit1–OE and DTA, $n = 14$ mice). Comparison between day points in each group: Friedman test followed by pairwise comparison of Scheffé, $^{*}P < 0.05$, $^{**}P < 0.01$; comparison between TP Cnt and every other group at 77 days: Steel test, $^{\#}P < 0.05$, $^{\#\#}P < 0.01$. (**K**) Schematic summary of the findings. St, striatum; GP, globus pallidus; OB, olfactory bulb. Dot plots represent each value (small dot) with lines representing mean ± standard error of the mean.

revealed that the lentivirus-labeled transplant-derived neurons formed postsynaptic structures with a dense postsynaptic density (asymmetric synapses, which are typically excitatory synapses) in the striatum (Fig. 4N) and presynaptic structures in symmetric (typically inhibitory) synapses at their axonal terminals in the globus pallidus (Fig. 4O), similar to normal striatal projection neurons. Together, these data indicate that these new neurons were functionally integrated into the striatal circuitry in the poststroke brain.

Slit1 overexpression did not affect the total number of $NeuN^+$ mature neurons in the striatum that emigrated from the transplant (Cnt, 324 ± 131 cells, $n = 20$ mice; Slit1-OE, 307 ± 103 cells, $n = 21$ mice; $P > 0.05$) but significantly increased the percentage of $NeuN^+$ or $DARPP32^+$ mature neurons that moved more than 100 μm from the transplant site toward the lesion located at the lateral striatum (Fig. 4, P and Q, and fig. S4M). The proportion of lentivirus-labeled axons projecting into the lateral globus pallidus, where neurons in the lateral striatum preferentially project under physiological conditions, was significantly increased in the Slit1-OE group compared with the Cnt (Fig. 4, R and S), suggesting that the new neurons that were positioned close to the injured area functionally replaced the neurons lost by stroke.

Mice without cell transplantation exhibited stroke-induced asymmetric body movement in the elevated body swing test and foot-fault test for 5 weeks (Fig. 5, A to G, black lines). Notably, the transplantation of Slit1-OE but not Cnt cells significantly improved these neurological dysfunctions at 5 weeks after stroke (Fig. 5, A to C). To investigate the involvement of transplant-derived neurons in the functional recovery, we used the *NSE-DTA; Nestin-CreER* mouse line in which apoptosis is induced by diphtheria toxin subunit A (DTA) specifically in cells undergoing neuronal differentiation after tamoxifen injection (*24*) (fig. S4, N to Q) as a source for grafted cells. Eliminating the transplant-derived neurons using this system significantly suppressed the Slit1 overexpression–induced improvements in the neurological tests (Fig. 5, A to C, blue lines), suggesting that the neurological improvement due to Slit1 overexpression resulted from the transplant-derived neurons. Animals treated with Slit1-OE cells, but not with Cnt cells or DTA cells, showed significant improvement in the elevated body swing test and foot-fault test even at 77 days after stroke (10 weeks after cell transplantation; Fig. 5, H to J), suggesting that the effect of Slit1-OE cell transplantation on neurological recovery involves a persistent event lasting at least a few months. The levels of neurological recovery were positively correlated with the percentage of mature new neurons located close to the lesion (Fig. 5, F and G) rather than with the total number of these neurons surviving in the striatum (Fig. 5, D and E), suggesting that the appropriately positioned regenerated neurons efficiently contributed to functional recovery.

DISCUSSION

Here, using *Gfap-EGFP* mice and SBF-SEM, which can reveal the morphology of astrocytes very precisely, we found that migrating neuroblasts in the poststroke striatum were enwrapped in the processes of reactive astrocytes, even in the areas without neuronal loss (Fig. 1, A to C). In the RMS, the physiological migratory path toward the olfactory bulbs, astrocytes promote neuroblast migration by forming tunnels, and this tunnel formation is controlled by neuroblast-derived Slit1 (*11*). On the other hand, our time-lapse imaging analyses showed that these astrocytes interfere with the migration of neuroblasts approaching a lesion. Compared to those in the RMS, the astrocytic processes in the poststroke striatum extended more irregularly and extensively. Slit1 deletion in neuroblasts or Robo2 knockdown in reactive astrocytes further inhibited the migration of neuroblasts toward the lesion (Fig. 2), suggesting that Slit1 helps neuroblasts to migrate through the reactive astrocytes. The 3D-reconstructed image from SBF-SEM data (Fig. 3A) and time-lapse images of astrocytes embedded in 3D gels (Fig. 3, B to E) indicated that the formation of thin protrusions on the astrocyte surface is suppressed by migrating neuroblasts using Slit1. While the Slit1 expression in neuroblasts was down-regulated in the poststroke striatum compared with that in the V-SVZ (fig. S1, F and G), their lentivirus-mediated overexpression of Slit1 significantly improved their migration toward the lesion (fig. S4, A to G). These results together indicated that the rearrangement of actin cytoskeleton in reactive astrocytes mediated by Slit-Robo signaling is a critical process for the efficient migration of neuroblasts in the injured brain.

Considering that there are similarities in the dynamic cytoskeletal modifications associated with neuronal migration and axonal growth, there might be common mechanisms in the neuroblast migration toward a lesion and the axonal regrowth beyond the injury. In axonal regeneration after spinal cord injury, the role of the reactive astrocytes that form the glial scar surrounding the lesion is still controversial (*25*, *26*). While they produce molecules that suppress axonal regrowth, they also produce factors that promote regrowth and themselves appear to provide scaffolds for the axons. Although reactive astrocytes are known to support neuroblast migration by producing chemoattractants (*27*, *28*), they also inhibit neuronal migration toward a lesion, as shown in this study (Figs. 1 and 2 and figs. S1 and S2). Therefore, by suppressing their inhibitory effect, which we achieved by up-regulating the Slit-Robo signaling, reactive astrocytes may act to promote neuronal regeneration.

We and others have previously reported that migrating neuroblasts are closely associated with blood vessels in the poststroke striatum (*6*, *13*–*16*, *29*). Although vascular endothelial cells express Robo proteins (*30*), these blood vessels are frequently surrounded by thin processes of astrocytes (Fig. 1, A and A″) (*6*, *13*, *16*), suggesting that neuroblasts directly interact with astrocytes rather than with endothelial cells or basement membrane when they migrate along vascular scaffolds. The density of blood vessels was not significantly altered in the striatum of *Slit1*-KO mice (fig. S2, L and M), although Slit-Robo signaling is reported to be involved in angiogenesis (*30*). Given that Robo2 was distributed in the processes of the reactive astrocytes that enwrapped blood vessels in the poststroke striatum and that the *Slit1*-KO neuroblasts formed aggregates with an irregular morphology when in contact with blood vessels (fig. S2M), it is possible that the Slit-Robo–mediated mechanism for clearing astrocytic processes is also involved in the blood vessel–guided neuroblast migration.

The molecular mechanisms regulating the Slit1 expression level in neuroblasts remain to be elucidated. Similar to that in the poststroke striatum, the Slit1 expression in V-SVZ–derived neuroblasts was rapidly decreased in the olfactory bulb, where the neuroblasts leave the stem/progenitor niche and differentiate into mature neurons (fig. S1I). Therefore, unknown factors provided in the specific environmental niche may be involved in maintaining the Slit1 expression in neuroblasts. It is also possible that the Slit1 expression depends on the immature and/or migratory status of the

neuroblasts and then decreases in cells under differentiation. On the other hand, the Robo2 expression was significantly increased in the striatal astrocytes after stroke (Fig. 1F and fig. S1L). It was previously reported that placental cells exposed to hypoxia have increased Robo expression (*31*). Consistent with that finding, our in vitro experiments using dissociated striatal astrocytes showed that the Robo2 mRNA was significantly increased 4 days after hypoxia exposure (fig. S2I), suggesting that hypoxic stimulation triggers an up-regulation of Robo2 in the poststroke striatal astrocytes. Further studies are needed to elucidate the molecular mechanisms regulating Slit-Robo signaling in the poststroke brain.

Currently, stem/progenitor cell transplantation has attracted much attention as a novel therapy for stroke and some neurodegenerative diseases. While its beneficial effects on functional regeneration reported in most previous studies depended on trophic effects of the transplanted cells, some studies have demonstrated that grafted cells derived from embryonic or induced pluripotent stem cells into the lesion differentiate into neurons and integrate into the host neuronal circuitry in the striatum and/or the neocortex (*32*–*34*). While the proliferation, survival, and differentiation of the transplanted cells have been well investigated, the mechanism of their migration and its effect on functional rewiring have not been focused upon. In this study, we used the postnatal V-SVZ as the source of grafted cells (Figs. 4 and 5). When the cells were transplanted directly into the lesion core in the lateral striatum, most of them differentiated into astrocytes (fig. S4R) and not into striatal neurons. Using two neurological tests in which performance defects have been reported in animals injured only within the striatum (*35*–*38*), we demonstrated here that V-SVZ cells transplanted into the medial striatum induced delayed and persistent functional recovery only when the transplant-derived neuroblasts, using Slit1, efficiently migrated through the reactive astrocytes to a position near the lesion. Since the neurons in different striatal areas have distinct synaptic partners and functions (*39*), methods for controlling the position of new neurons may be critical for functional regeneration. Slit1 overexpression increased the proportion of transplant-derived mature new neurons that became closely positioned to the lesion at the lateral striatum, which resulted in the appropriate axonal projection into the physiological target area, the lateral globus pallidus (Fig. 5K). Although the precise mechanisms of the observed recovery in motor functions remain to be elucidated, we demonstrated that these regenerated neurons were efficiently integrated into the circuitry and contributed to functional improvement.

The approach presented here manipulated only the neuroblasts/new neurons, and not the reactive astrocytes, which have various essential functions in neuronal regeneration (*40*). Reactive astrocytes, endothelial cells, and activated microglia have all been reported to be involved in redirecting neuroblasts toward an injured area by secreting attractive molecules (*14*, *27*, *28*). For the efficient recruitment of neuroblasts to a lesion, the direction of their migration needs to be determined by these mechanisms in addition to the clearance of their passage using Slit1. It will also be important to investigate how to overcome the decreased neurogenesis in the V-SVZ and the greater distance between the ventricular wall and striatum in the adult human brain compared with those in mice (*41*–*44*) in future studies. This study highlights the importance of controlling the migration and final positioning of regenerated neurons (Fig. 5K), in addition to cell proliferation and survival, for successful stem cell–based therapies.

MATERIALS AND METHODS

Animals

Male 9- to 12-week-old Institute of Cancer Research mice were purchased from SLC (Shizuoka, Japan). *Slit1* mutant mice (*45*), *Slit1* reporter mice (*46*), *Dcx-DsRed* transgenic mice (*47*), *NSE-DTA* transgenic mice (*24*), *Nestin-CreER* transgenic mice (*48*), and *Gfap-EGFP* mice and *Dcx-EGFP* mice (*49*) were described previously. Sample sizes were estimated on the basis of previous studies using similar experimental designs. No statistical methods were used to predetermine sample size. All experiments using live animals were performed in accordance with the guidelines and regulations of Nagoya City University and the National Institute for Physiological Sciences.

Induction of ischemic stroke

Mice (9 to 12 weeks old) were anesthetized with an oxygen/isoflurane mixture (97.5/2.5%) administered through an inhalation mask and placed on a 37°C heating bed. Middle cerebral artery occlusion was induced by the intraluminal filament technique, as reported previously (*50*) with several modifications. After fixation, the brain sections were immunostained for the mature neuronal marker NeuN to examine the extent of the infarcted area with neuronal loss. Only the individuals with an infarction area covering 10 to 30% of the ipsilateral hemisphere were used for analysis. About 50% of the animals subjected to the surgery met this criterion. For details, see the Supplementary Materials.

Robo2 knockdown

Robo2-shRNA–encoding lentivirus was prepared as previously described (*11*), using packaging and envelope plasmids (Addgene plasmid #12260 and #12259) and a lentivirus vector encoding *Robo2* shRNA or a Cnt shRNA with a nontarget sequence (Open Biosystems, Huntsville, AL, USA). Each animal was given stereotaxic injections of 1.8 μl of lentivirus into the medial striatum of the right hemisphere (relative to bregma: anterior, 0.9 mm; lateral, 1.25 mm; depth, 2.6 to 2.0 mm) 2 days before stroke induction and then was fixed 20 days later.

Construction of a Slit1-overexpression vector

Human *Slit1* complementary DNA (cDNA) cloned into the *pCR-XL-TOPO* vector (Thermo Fisher Scientific, Waltham, MA, USA) was inserted into pENTR2B (Invitrogen, Carlsbad, CA, USA) at the Eco RI site, which was then transferred into the *CS2-CMV-RfA-IRES2-Venus* lentiviral vector (provided by H. Miyoshi, RIKEN, Wako, Japan) using the Gateway system (Invitrogen). As a Cnt, the same vector into which DsRed cDNA was inserted using the Gateway system or the *CS2-CMV-Venus* lentiviral vector (provided by H. Miyoshi) was used. For time-lapse imaging, the *Slit1* cDNA was inserted into the *LeGO-iT* lentivirus vector (Addgene plasmid #27361; a gift from B. Fehse) (*51*) at the Eco RI site.

Transplantation of V-SVZ cells

For transplantation experiments, the V-SVZ of postnatal day (P)1-6 WT, *Dcx-EGFP*, *Slit1*-KO;*Dcx-EGFP*, or *NSE-DTA;Nestin-CreER* mice that had received a tamoxifen injection (20 mg/kg, intraperitoneally 1 day before; Sigma-Aldrich, St. Louis, MO, USA) was dissected and dissociated using trypsin-EDTA (Invitrogen) as previously described (*11*). For Slit1-overexpression experiments, *Slit1*-expressing or Cnt lentivirus was diluted three times with distilled phosphate-buffered saline (PBS), and the supernatant was collected after centrifugation

at 1000*g* for 10 min at 4°C to completely remove the precipitates. V-SVZ cells were incubated with the lentivirus-containing supernatant for 90 min on ice, washed with L15 medium containing deoxyribonuclease 1 (20 U/ml; Roche, Basel, Switzerland), and then resuspended in L15. With this method, none of the host DARPP32$^+$ striatal projection neurons around the transplanted area was labeled with the lentivirus when fixed within 10 days after transplantation, suggesting that host cells were not directly infected with the lentiviruses carried in the cell suspensions for transplantation.

The animals were successively assigned to treatment groups 1 day or just before transplantation. Because the amount of body weight loss in the first 7 days after stroke can reflect the stroke size, the animals were ranked according to their body weight loss and then assigned to groups so that the mean body weight loss in each group was about the same. The cell suspension (3.2 μl) was stereotaxically injected into the ipsilateral medial striatum (relative to bregma: anterior, 1.3 mm; lateral, 1.35 mm; depth, 2.6 to 2.0 mm) of mice 8 days (Figs. 4 and 5 and fig. S4, F, G, and J) or 10 to 12 days (Fig. 2, H to K, and fig. S4, C to E) after stroke. Since stroke-induced tissue atrophy could prevent targeted injection into the striatum, the injection site in each animal was checked using brain sections prepared as described below. Mice in which more than 30% of the transplanted cells were distributed outside the medial striatum (for example, the lateral ventricle, medial septum, and/or neocortex) or inside the infarct tissue were excluded from the analyses.

Retrograde neuronal tracer injection

To label the transplant-derived neurons projected into the globus pallidus, 0.3 μl of 0.5% Alexa Fluor 647–conjugated cholera toxin subunit B (Invitrogen, Carlsbad, CA, USA), a retrograde axonal tracer, dissolved in PBS was stereotaxically injected into the globus pallidus of the poststroke mice 4 weeks after V-SVZ cell transplantation. Four days later, the animals were fixed. For details, see the Supplementary Materials.

Time-lapse imaging of poststroke brain slices

Brain slices for time-lapse imaging were prepared from adult 10- to 16-day poststroke *Gfap-EGFP;Dcx-DsRed* mice or from poststroke *Gfap-EGFP* mice 5 days after the transplantation of lentivirus-labeled V-SVZ cells into the medial striatum, as reported previously (*16*), with modifications. The slices were placed on a stage-top imaging chamber under continuous perfusion of artificial cerebrospinal fluid during the imaging using a confocal laser microscope (LSM710, Carl Zeiss, Jena, Thuringia, Germany) for 8 to 18 hours.

To quantify the neuroblasts' migration speed, neuroblasts in the striatum in the captured images were traced using ImageJ software (manual tracking plugin). Only the neuroblasts that could be continuously tracked for at least 40 min were used for this analysis. For details, see the Supplementary Materials.

Immunohistochemistry

Cell proliferation in the V-SVZ, neuroblast migration, and neuronal maturation in the injured striatum were analyzed in 7-, 18-, and 35-day poststroke mice, respectively. Animals were deeply anesthetized and perfused transcardially with PBS, followed by 4% paraformaldehyde (PFA) in 0.1 M phosphate buffer (PB). Brain sections were prepared and stained as previously described (*11*). For quantification, images were captured using an optical microscope (BX-51, Olympus, Tokyo, Japan) or a confocal laser microscope (LSM700, Carl Zeiss, Jena, Germany). For details, see the Supplementary Materials.

Transmission electron microscopy

Mice at 12 to 14 days after stroke were perfused transcardially with 20 ml of PBS, followed by 50 ml of 2% PFA–2.5% glutaraldehyde (GA) in 0.1 M PB. Serial semithin sections (1.5 μm) and ultrathin sections (60 to 70 nm) were prepared, as previously described (*12*). For details, see the Supplementary Materials.

Immunoelectron microscopy

Mice underwent V-SVZ cell transplantation at 8 days after stroke and were fixed with 2% PFA–2.5% GA in 0.1 M PB at 35 days after stroke, and the brains were postfixed with the same fixative overnight and cut into 100-μm coronal sections using a vibratome (VT1200S, Leica). Sections were processed as previously described (*52*). For details, see the Supplementary Materials.

Serial block-face scanning electron microscopy

Observation with SBF-SEM and analyses of acquired data were performed as described previously with slight modifications (*53*, *54*). SBF-SEM of the neuroblast chains was performed using a Merlin scanning electron microscope (Carl Zeiss) equipped with a 3View in-chamber ultramicrotome system (Gatan, Pleasanton, CA, USA). Sequential images were processed using FIJI. Segmentation of the cell membrane was performed using Microscopy Image Browser (*55*). 3D reconstruction was performed using Amira software (Visualization Sciences Group). For details, see the Supplementary Materials.

Electrophysiology

To examine the electrophysiological properties of the transplant-derived cells that matured in the poststroke striatum, WT mice that had undergone transient middle cerebral artery occlusion at P10 to P14 were subjected to transplantation with V-SVZ cells that had been treated with the Cnt lentivirus encoding DsRed 5 to 7 days later. Four to five weeks after cell transplantation, electrophysiological recording was performed. The obtained data were analyzed using AxoGraph (AxoGraph Scientific). For details, see the Supplementary Materials. After the recordings, the slices containing cells that were intracellularly labeled with biocytin were fixed. The neurons labeled with biocytin were visualized by the avidin-biotin–horseradish peroxidase reaction.

Neurological testing

WT mice were repeatedly subjected to quantitative neurological testing every week after stroke for 5 weeks (Fig. 5, A to C), or on the 1st, 5th, and 11th week after stroke (Fig. 5, H to J). The investigators were blinded to the treatments during the testing.

The foot-fault test was performed as previously described with modifications (*56*). The percentages of foot faults were calculated. For details, see the Supplementary Materials.

The elevated body swing test was performed as previously described with modifications (*36*). The percentage of the number of right side swings to the total number of swings was calculated. For details, see the Supplementary Materials.

Hypoxia exposure of cultured striatal astrocytes

The striatum or the V-SVZ was dissected from P4 to P7 WT mice and cultured as previously described (*11*). To increase the GFAP and Robo2

expression, immediately after changing the medium to FreeStyle (Thermo Fisher Scientific) containing penicillin/streptomycin (50 U/ml), the striatal astrocytes were incubated under 0 to 2% O_2 (AnaeroPack Kenki, Mitsubishi Gas Chemical Company, Tokyo, Japan) for 20 hours and then cultured in Dulbecco's modified Eagle's medium containing 10% fetal bovine serum, penicillin/streptomycin (50 U/ml), and 2 mM L-glutamine for 0 to 4 days, depending on the experiment.

Coculture of V-SVZ–derived neuroblasts with striatal astrocytes

After hypoxia exposure, the striatal astrocytes were kept under normal culture conditions for 2 days and then dissociated from the dishes using trypsin-EDTA (Invitrogen). The cells were resuspended in Nucleofector solution with 5 μg of plasmid and then subjected to nucleofection (Amaxa, Lonza, Basel, Switzerland). The cells were plated on glass-bottom dishes and then cultured for two overnights. The V-SVZ dissected from P0 to P3 WT and *Slit1*-KO mice for time-lapse imaging or from *Dcx-DsRed* mice crossed with *Slit1*-KO mouse lines for fixed imaging was cut into 150- to 200-μm-diameter pieces and plated on a monolayer culture of astrocytes. The cultures were then placed in the incubator overnight and then used for time-lapse imaging or fixed with 4% PFA.

In the 3D culture experiment, astrocytes subjected to nucleofection were incubated at 37°C for 6 to 8 hours on a laminin-coated dish, dissociated, and resuspended in a neutralized collagen solution (Purecol, Advanced BioMatrix, San Diego, CA, USA). For details, see the Supplementary Materials.

Lifeact imaging

Plasmids containing Lifeact-EGFP or Lifeact-mCherry were used to visualize polymerized actin in astrocytes (*17*, *57*). Time-lapse images of striatal astrocytes cocultured with V-SVZ–derived neuroblasts were automatically captured. Changes in the EGFP or mCherry level in the astrocytes during and after contact with migrating neuroblasts compared to the level before contact were analyzed using MetaMorph software (Molecular Devices). To examine the role of Cdc42 in the neuroblast-induced inhibition of actin polymerization, the astrocytes were cotransfected with Lifeact-mCherry and GFP-tagged WT (WT-*Cdc42*) or CA-*Cdc42* (provided by K. Kaibuchi). In the time-lapse imaging of thin-protrusion formation on the astrocytes embedded in collagen gels, the images were captured every 3 min for 2 to 5 hours. For details, see the Supplementary Materials.

FRET imaging

FRET-based imaging of the RhoA, Rac1, or Cdc402 activity in striatal astrocytes using FRET probes for each of these molecules (*19*) was performed essentially as described previously (*58*). Time-lapse images of striatal astrocytes cocultured with neuroblasts were automatically captured at 6-min intervals for 6 to 12 hours. Migrating neuroblasts were distinguished by their typical bipolar morphology in differential interference contrast images captured using a transmitted light detector. MetaMorph software (Molecular Devices) was used to represent the FRET level, which was calculated by the following equation: FRET level = intensity of FRET/cyan fluorescent protein. The average FRET level of each region before, during, and after contacting a migrating neuroblast was calculated and normalized by dividing it by the mean value of the frame just before the contact. For details, see the Supplementary Materials.

Statistics

At least three independent experiments were performed for each quantification. All data were expressed as the mean ± standard error of the mean. Normality and equal variances between group samples were assessed using the Shapiro-Wilk test and *F* test, respectively. When normality and equal variance between sample groups were achieved, differences between means were determined by a two-tailed Student's *t* test, paired *t* test, or one-way ANOVA, followed by a Dunnett's multiple comparison test or Bonferroni test. Where the normality or equal variance of samples failed, a two-tailed Mann-Whitney *U* test, Wilcoxon signed-rank test, Steel-Dwass test, Steel test, or Friedman test followed by Scheffé's multicomparison test was performed. A P value of <0.05 was considered to be statistically significant. Box plots show the median (dot), upper and lower quartiles (box), maximal and minimal values excluding outliers (whiskers), and outliers (blue squares). Dot plots show each value (small dots), and line graph values represent the mean ± standard error of the mean.

SUPPLEMENTARY MATERIALS

Supplementary material for this article is available at http://advances.sciencemag.org/cgi/content/full/4/12/eaav0618/DC1

Supplementary Materials and Methods

Fig. S1. Neuroblast migration in the 18-day poststroke brain.

Fig. S2. Impaired neuroblast migration by Slit-Robo signaling inhibition.

Fig. S3. Neuroblast-induced cytoskeletal modification in reactive astrocytes.

Fig. S4. Effects of Slit1 overexpression on the migration, proliferation, and apoptosis of neuroblasts.

Movie S1. SBF-SEM and 3D-reconstructed images of migrating neuroblasts and surrounding astrocytes in the poststroke brain.

Movie S2. Time-lapse imaging of migrating neuroblasts and reactive astrocytes in a poststroke brain slice.

Movie S3. Time-lapse imaging of neuroblasts migrating in a reactive astrocyte–enriched area in poststroke brain slices.

Movie S4. Altered actin polymerization in astrocytes making contact with migrating neuroblasts.

Movie S5. Alteration in Cdc42 activity in astrocytes induced by neuroblast contact.

Movie S6. Dynamic alteration of Cdc42 activity and protrusion formation at the surface of astrocytes.

Movie S7. Time-lapse imaging of Cnt and *Slit1*-OE neuroblasts in the poststroke brain.

References (*59*, *60*)

REFERENCES AND NOTES

1. R. A. Ihrie, A. Álvarez-Buylla, Lake-front property: A unique germinal niche by the lateral ventricles of the adult brain. *Neuron* **70**, 674–686 (2011).
2. N. Kaneko, M. Sawada, K. Sawamoto, Mechanisms of neuronal migration in the adult brain. *J. Neurochem.* **141**, 835–847 (2017).
3. D. A. Lim, A. Alvarez-Buylla, The adult ventricular-subventricular zone (V-SVZ) and olfactory bulb (OB) neurogenesis. *Cold Spring Harb. Perspect. Biol.* **8**, a018820 (2016).
4. A. Arvidsson, T. Collin, D. Kirik, Z. Kokaia, O. Lindvall, Neuronal replacement from endogenous precursors in the adult brain after stroke. *Nat. Med.* **8**, 963–970 (2002).
5. J. M. Parent, Z. S. Vexler, C. Gong, N. Derugin, D. M. Ferriero, Rat forebrain neurogenesis and striatal neuron replacement after focal stroke. *Ann. Neurol.* **52**, 802–813 (2002).
6. T. Yamashita, M. Ninomiya, P. Hernández Acosta, J. M. Garcia-Verdugo, T. Sunabori, M. Sakaguchi, K. Adachi, T. Kojima, Y. Hirota, T. Kawase, N. Araki, K. Abe, H. Okano, K. Sawamoto, Subventricular zone-derived neuroblasts migrate and differentiate into mature neurons in the post-stroke adult striatum. *J. Neurosci.* **26**, 6627–6636 (2006).
7. B. S. Khakh, M. V. Sofroniew, Diversity of astrocyte functions and phenotypes in neural circuits. *Nat. Neurosci.* **18**, 942–952 (2015).
8. M. V. Sofroniew, Astrogliosis. *Cold Spring Harb. Perspect. Biol.* **7**, a020420 (2015).
9. Y. Li, Z. Liu, H. Xin, M. Chopp, The role of astrocytes in mediating exogenous cell-based restorative therapy for stroke. *Glia* **62**, 1–16 (2014).
10. A. Gengatharan, R. R. Bammann, A. Saghatelyan, The role of astrocytes in the generation, migration, and integration of new neurons in the adult olfactory bulb. *Front. Neurosci.* **10**, 149 (2016).
11. N. Kaneko, O. Marín, M. Koike, Y. Hirota, Y. Uchiyama, J. Y. Wu, Q. Lu, M. Tessier-Lavigne, A. Alvarez-Buylla, H. Okano, J. L. Rubenstein, K. Sawamoto, New neurons clear the path of

astrocytic processes for their rapid migration in the adult brain. *Neuron* **67**, 213–223 (2010).
12. F. Doetsch, J. M. García-Verdugo, A. Alvarez-Buylla, Cellular composition and three-dimensional organization of the subventricular germinal zone in the adult mammalian brain. *J. Neurosci.* **17**, 5046–5061 (1997).
13. T. Kojima, Y. Hirota, M. Ema, S. Takahashi, I. Miyoshi, H. Okano, K. Sawamoto, Subventricular zone-derived neural progenitor cells migrate along a blood vessel scaffold toward the post-stroke striatum. *Stem Cells* **28**, 545–554 (2010).
14. J. J. Ohab, S. Fleming, A. Blesch, S. T. Carmichael, A neurovascular niche for neurogenesis after stroke. *J. Neurosci.* **26**, 13007–13016 (2006).
15. R. L. Zhang, M. Chopp, S. R. Gregg, Y. Toh, C. Roberts, Y. LeTourneau, B. Buller, L. Jia, S. P. Nejad Davarani, Z. G. Zhang, Patterns and dynamics of subventricular zone neuroblast migration in the ischemic striatum of the adult mouse. *J. Cereb. Blood Flow Metab.* **29**, 1240–1250 (2009).
16. S. Grade, Y. C. Weng, M. Snapyan, J. Kriz, J. O. Malva, A. Saghatelyan, Brain-derived neurotrophic factor promotes vasculature-associated migration of neuronal precursors toward the ischemic striatum. *PLOS ONE* **8**, e55039 (2013).
17. J. Riedl, A. H. Crevenna, K. Kessenbrock, J. H. Yu, D. Neukirchen, M. Bista, F. Bradke, D. Jenne, T. A. Holak, Z. Werb, M. Sixt, R. Wedlich-Soldner, Lifeact: A versatile marker to visualize F-actin. *Nat. Methods* **5**, 605–607 (2008).
18. A. Hall, Rho GTPases and the actin cytoskeleton. *Science* **279**, 509–514 (1998).
19. H. Yoshizaki, Y. Ohba, K. Kurokawa, R. E. Itoh, T. Nakamura, N. Mochizuki, K. Nagashima, M. Matsuda, Activity of Rho-family GTPases during cell division as visualized with FRET-based probes. *J. Cell Biol.* **162**, 223–232 (2003).
20. S. Bardehle, M. Krüger, F. Buggenthin, J. Schwausch, J. Ninkovic, H. Clevers, H. J. Snippert, F. J. Theis, M. Meyer-Luehmann, I. Bechmann, L. Dimou, M. Götz, Live imaging of astrocyte responses to acute injury reveals selective juxtavascular proliferation. *Nat. Neurosci.* **16**, 580–586 (2013).
21. Y. Kawaguchi, C. J. Wilson, P. C. Emson, Intracellular recording of identified neostriatal patch and matrix spiny cells in a slice preparation preserving cortical inputs. *J. Neurophysiol.* **62**, 1052–1068 (1989).
22. T. Kita, H. Kita, S. T. Kitai, Passive electrical membrane properties of rat neostriatal neurons in an in vitro slice preparation. *Brain Res.* **300**, 129–139 (1984).
23. Y. Kawaguchi, C. J. Wilson, P. C. Emson, Projection subtypes of rat neostriatal matrix cells revealed by intracellular injection of biocytin. *J. Neurosci.* **10**, 3421–3438 (1990).
24. K. Kobayakawa, R. Kobayakawa, H. Matsumoto, Y. Oka, T. Imai, M. Ikawa, M. Okabe, T. Ikeda, S. Itohara, T. Kikusui, K. Mori, H. Sakano, Innate versus learned odour processing in the mouse olfactory bulb. *Nature* **450**, 503–508 (2007).
25. M. A. Anderson, J. E. Burda, Y. Ren, Y. Ao, T. M. O'Shea, R. Kawaguchi, G. Coppola, B. S. Khakh, T. J. Deming, M. V. Sofroniew, Astrocyte scar formation aids central nervous system axon regeneration. *Nature* **532**, 195–200 (2016).
26. M. Hara, K. Kobayakawa, Y. Ohkawa, H. Kumamaru, K. Yokota, T. Saito, K. Kijima, S. Yoshizaki, K. Harimaya, Y. Nakashima, S. Okada, Interaction of reactive astrocytes with type I collagen induces astrocytic scar formation through the integrin–N-cadherin pathway after spinal cord injury. *Nat. Med.* **23**, 818–828 (2017).
27. A. M. Robin, Z. G. Zhang, L. Wang, R. L. Zhang, M. Katakowski, L. Zhang, Y. Wang, C. Zhang, M. Chopp, Stromal cell-derived factor 1α mediates neural progenitor cell motility after focal cerebral ischemia. *J. Cereb. Blood Flow Metab.* **26**, 125–134 (2006).
28. Y.-P. Yan, K. A. Sailor, B. T. Lang, S.-W. Park, R. Vemuganti, R. J. Dempsey, Monocyte chemoattractant protein-1 plays a critical role in neuroblast migration after focal cerebral ischemia. *J. Cereb. Blood Flow Metab.* **27**, 1213–1224 (2007).
29. T. Fujioka, N. Kaneko, I. Ajioka, K. Nakaguchi, T. Omata, H. Ohba, R. Fässler, J. M. García-Verdugo, K. Sekiguchi, N. Matsukawa, K. Sawamoto, β1 integrin signaling promotes neuronal migration along vascular scaffolds in the post-stroke brain. *EBioMedicine* **16**, 195–203 (2017).
30. H. Blockus, A. Chédotal, Slit-Robo signaling. *Development* **143**, 3037–3044 (2016).
31. W.-X. Liao, L. C. Laurent, S. Agent, J. Hodges, D.-b. Chen, Human placental expression of SLIT/ROBO signaling cues: Effects of preeclampsia and hypoxia. *Biol. Reprod.* **86**, 111 (2012).
32. Z. Kokaia, D. Tornero, O. Lindvall, Transplantation of reprogrammed neurons for improved recovery after stroke. *Prog. Brain Res.* **231**, 245–263 (2017).
33. C. Reis, M. Wilkinson, H. Reis, O. Akyol, V. Gospodarev, C. Araujo, S. Chen, J. H. Zhang, A look into stem cell therapy: Exploring the options for treatment of ischemic stroke. *Stem Cells Int.* **2017**, 3267352 (2017).
34. Y. Zhang, H. Yao, Potential therapeutic mechanisms and tracking of transplanted stem cells: Implications for stroke treatment. *Stem Cells Int.* **2017**, 2707082 (2017).
35. C. V. Borlongan, T. S. Randall, D. W. Cahill, P. R. Sanberg, Asymmetrical motor behavior in rats with unilateral striatal excitotoxic lesions as revealed by the elevated body swing test. *Brain Res.* **676**, 231–234 (1995).
36. C. V. Borlongan, P. R. Sanberg, Elevated body swing test: A new behavioral parameter for rats with 6-hydroxydopamine-induced hemiparkinsonism. *J. Neurosci.* **15**, 5372–5378 (1995).
37. M. Roghani, G. Behzadi, T. Baluchnejadmojarad, Efficacy of elevated body swing test in the early model of Parkinson's disease in rat. *Physiol. Behav.* **76**, 507–510 (2002).
38. L. Zhang, T. Schallert, Z. G. Zhang, Q. Jiang, P. Arniego, Q. Li, M. Lu, M. Chopp, A test for detecting long-term sensorimotor dysfunction in the mouse after focal cerebral ischemia. *J. Neurosci. Methods* **117**, 207–214 (2002).
39. P. Voorn, L. J. M. J. Vanderschuren, H. J. Groenewegen, T. W. Robbins, C. M. A. Pennartz, Putting a spin on the dorsal–ventral divide of the striatum. *Trends Neurosci.* **27**, 468–474 (2004).
40. M. V. Sofroniew, H. V. Vinters, Astrocytes: Biology and pathology. *Acta Neuropathol.* **119**, 7–35 (2010).
41. O. Bergmann, J. Liebl, S. Bernard, K. Alkass, M. S. Y. Yeung, P. Steier, W. Kutschera, L. Johnson, M. Landén, H. Druid, K. L. Spalding, J. Frisén, The age of olfactory bulb neurons in humans. *Neuron* **74**, 634–639 (2012).
42. N. Sanai, T. Nguyen, R. A. Ihrie, Z. Mirzadeh, H.-H. Tsai, M. Wong, N. Gupta, M. S. Berger, E. Huang, J.-M. Garcia-Verdugo, D. H. Rowitch, A. Alvarez-Buylla, Corridors of migrating neurons in the human brain and their decline during infancy. *Nature* **478**, 382–386 (2011).
43. C. Wang, F. Liu, Y.-Y. Liu, C.-H. Zhao, Y. You, L. Wang, J. Zhang, B. Wei, T. Ma, Q. Zhang, Y. Zhang, R. Chen, H. Song, Z. Yang, Identification and characterization of neuroblasts in the subventricular zone and rostral migratory stream of the adult human brain. *Cell Res.* **21**, 1534–1550 (2011).
44. M. F. Paredes, S. F. Sorrells, J. M. Garcia-Verdugo, A. Alvarez-Buylla, Brain size and limits to adult neurogenesis. *J. Comp. Neurol.* **524**, 646–664 (2016).
45. A. S. Plump, L. Erskine, C. Sabatier, K. Brose, C. J. Epstein, C. S. Goodman, C. A. Mason, M. Tessier-Lavigne, Slit1 and Slit2 cooperate to prevent premature midline crossing of retinal axons in the mouse visual system. *Neuron* **33**, 219–232 (2002).
46. K. T. Nguyen-Ba-Charvet, N. Picard-Riera, M. Tessier-Lavigne, A. Baron-Van Evercooren, C. Sotelo, A. Chédotal, Multiple roles for slits in the control of cell migration in the rostral migratory stream. *J. Neurosci.* **24**, 1497–1506 (2004).
47. X. Wang, R. Qiu, W. Tsark, Q. Lu, Rapid promoter analysis in developing mouse brain and genetic labeling of young neurons by doublecortin-DsRed-express. *J. Neurosci. Res.* **85**, 3567–3573 (2007).
48. I. Imayoshi, T. Ohtsuka, D. Metzger, P. Chambon, R. Kageyama, Temporal regulation of Cre recombinase activity in neural stem cells. *Genesis* **44**, 233–238 (2006).
49. S. Gong, C. Zheng, M. L. Doughty, K. Losos, N. Didkovsky, U. B. Schambra, N. J. Nowak, A. Joyner, G. Leblanc, M. E. Hatten, N. Heintz, A gene expression atlas of the central nervous system based on bacterial artificial chromosomes. *Nature* **425**, 917–925 (2003).
50. H. Hara, P. L. Huang, N. Panahian, M. C. Fishman, M. A. Moskowitz, Reduced brain edema and infarction volume in mice lacking the neuronal isoform of nitric oxide synthase after transient MCA occlusion. *J. Cereb. Blood Flow Metab.* **16**, 605–611 (1996).
51. K. Weber, U. Bartsch, C. Stocking, B. Fehse, A multicolor panel of novel lentiviral "gene ontology" (LeGO) vectors for functional gene analysis. *Mol. Ther.* **16**, 698–706 (2008).
52. M. S. Sirerol-Piquer, A. Cebrián-Silla, C. Alfaro-Cervelló, U. Gomez-Pinedo, M. Soriano-Navarro, J.-M. G. Verdugo, GFP immunogold staining, from light to electron microscopy, in mammalian cells. *Micron* **43**, 589–599 (2012).
53. H. B. Nguyen, T. Q. Thai, S. Saitoh, B. Wu, Y. Saitoh, S. Shimo, H. Fujitani, H. Otobe, N. Ohno, Conductive resins improve charging and resolution of acquired images in electron microscopic volume imaging. *Sci. Rep.* **6**, 23721 (2016).
54. T. Q. Thai, H. B. Nguyen, S. Saitoh, B. Wu, Y. Saitoh, S. Shimo, Y. H. Elewa, O. Ichii, Y. Kon, T. Takaki, K. Joh, N. Ohno, Rapid specimen preparation to improve the throughput of electron microscopic volume imaging for three-dimensional analyses of subcellular ultrastructures with serial block-face scanning electron microscopy. *Med. Mol. Morphol.* **49**, 154–162 (2016).
55. I. Belevich, M. Joensuu, D. Kumar, H. Vihinen, E. Jokitalo, Microscopy image browser: A platform for segmentation and analysis of multidimensional datasets. *PLOS Biol.* **14**, e1002340 (2016).
56. T. D. Hernandez, T. Schallert, Seizures and recovery from experimental brain damage. *Exp. Neurol.* **102**, 318–324 (1988).
57. S. Yamashiro, H. Mizuno, M. B. Smith, G. L. Ryan, T. Kiuchi, D. Vavylonis, N. Watanabe, New single-molecule speckle microscopy reveals modification of the retrograde actin flow by focal adhesions at nanometer scales. *Mol. Biol. Cell* **25**, 1010–1024 (2014).
58. H. Ota, T. Hikita, M. Sawada, T. Nishioka, M. Matsumoto, M. Komura, A. Ohno, Y. Kamiya, T. Miyamoto, N. Asai, A. Enomoto, M. Takahashi, K. Kaibuchi, K. Sobue, K. Sawamoto, Speed control for neuronal migration in the postnatal brain by Gmip-mediated local inactivation of RhoA. *Nat. Commun.* **5**, 4532 (2014).
59. A. Tamada, T. Kumada, Y. Zhu, T. Matsumoto, Y. Hatanaka, K. Muguruma, Z. Chen, Y. Tanabe, M. Torigoe, K. Yamauchi, H. Oyama, K. Nishida, F. Murakami, Crucial roles of Robo proteins in midline crossing of cerebellofugal axons and lack of their up-regulation after midline crossing. *Neural Dev.* **3**, 29 (2008).
60. L.-S. Zheng, N. Kaneko, K. Sawamoto, Minocycline treatment ameliorates interferon-alpha-induced neurogenic defects and depression-like behaviors in mice. *Front. Cell. Neurosci.* **9**, 5 (2015).

Acknowledgments: We thank M. Matsuda for the small GTPase biosensors, N. Watanabe for the Lifeact plasmid, K. Kaibuchi for the WT and mutant Cdc42 expression vectors, H. Miyoshi for the *CS2-CMV-Venus* lentiviral vector, F. Murakami for the Robo2 antibody, Q. Lu for the *Dcx-DsRed* mice, S. Itohara for the *NES-DTA* mice, and H. Oishi, I. Miyoshi, T. Miyamoto, K. Ikenaka, M. Furuse, and K. Kobayashi for technical support. **Funding:** This work was supported by research grants from NEXT (LS104), MEXT KAKENHI [22122004, 17H05750, and 17H05512 (to K.S.) and 15H05873 (to A.N.)], JSPS KAKENHI [26250019, 17H01392, and JP16H06280 (to K.S.); 25111727, 23680041, and 17K07114 (to N.K.); and 26250009 (to A.N.)], the JSPS Program for Advancing Strategic International Networks to Accelerate the Circulation of Talented Researchers [S2704 (to N.K., V.H.-P., J.M.G.-V., and K.S.)], the Brain Science Foundation (to N.K.), a Grant-in-Aid for Research at Nagoya City University (to N.K. and K.S.), GVA Prometeoll/2014/075 (to J.M.G.-V.), TerCel ISCIII2012-RED-19-016 (to J.M.G.-V.), the Takeda Science Foundation (to K.S.), and the Cooperative Study Programs of the National Institute for Physiological Sciences (to N.K. and K.S.). **Author contributions:** N.K. performed all the experiments. T.Ot. and H.S. performed electrophysiological experiments. T.Om. performed neurological assessments. V.H.-P. and J.M.G.-V. performed transmission electron microscopy. N.K., N.O., H.B.N., and T.Q.T. performed 3D SEM. N.K. and K.S. wrote the manuscript. N.K., Y.K., A.N., J.M.G.-V., and K.S. designed the experiments. K.S. supervised the whole project. **Competing interests:** The authors declare that they have no competing interests. **Data and materials availability:** All data needed to evaluate the conclusions in the paper are present in the paper and/or the Supplementary Materials. Additional data related to this paper may be requested from the authors.

Submitted 10 August 2018
Accepted 11 November 2018
Published 12 December 2018
10.1126/sciadv.aav0618

Citation: N. Kaneko, V. Herranz-Pérez, T. Otsuka, H. Sano, N. Ohno, T. Omata, H. B. Nguyen, T. Q. Thai, A. Nambu, Y. Kawaguchi, J. M. García-Verdugo, K. Sawamoto, New neurons use Slit-Robo signaling to migrate through the glial meshwork and approach a lesion for functional regeneration. *Sci. Adv.* **4**, eaav0618 (2018).

New neurons use Slit-Robo signaling to migrate through the glial meshwork and approach a lesion for functional regeneration

N. Kaneko, V. Herranz-Pérez, T. Otsuka, H. Sano, N. Ohno, T. Omata, H. B. Nguyen, T. Q. Thai, A. Nambu, Y. Kawaguchi, J. M. García-Verdugo and K. Sawamoto

Sci Adv **4** (12), eaav0618.
DOI: 10.1126/sciadv.aav0618